Magnetic dipole and electric quadrupole rotational structures and chirality in ^{105}Rh

J. A. Alcántara-Núñez, J. R. B. Oliveira, E. W. Cybulska, N. H. Medina, M. N. Rao, R. V. Ribas, M. A. Rizzutto, W. A. Seale, F. Falla-Sotelo, and K. T. Wiedemann
Instituto de Física, Universidade de São Paulo, São Paulo, SP, Caixa Postal 05315-970, Brazil

V. I. Dimitrov* and S. Frauendorf
Department of Physics, University of Notre Dame, Notre Dame, Indiana 46556, USA
and Institute for Nuclear and Hadronic Physics, Research Center Rossendorf, P.O. Box 51 01 19, 01314 Dresden, Germany
(Received 14 July 2003; published 27 February 2004)

The ^{105}Rh nucleus has been studied with the ^{100}Mo(^{11}B, $\alpha 2n\gamma$) reaction at 43 MeV incident energy. A rich variety of structures was observed at high and low spins, using γ-γ-*t* and γ-γ-*particle* coincidences and directional correlation ratios. A γ-vibrational band was observed for the first time in this nucleus. A new structure based on the intruder $1/2^+$[431] proton orbital was identified. Four magnetic dipole bands have also been observed at high spin, three of which have negative parity and have similar characteristics: they are very regular in energy spacing, presenting nearly constant alignments and large values of $B(M1)/B(E2)$ ratios. Two of them are nearly degenerate in excitation energy and could be chiral partners. The $\pi g_{9/2} \otimes \nu h_{11/2}(g_{7/2}, d_{5/2})$ configuration is tentatively assigned for these bands, with the angular momenta of the proton and neutron intruders and the collective angular momentum aligning along the three perpendicular axes of the triaxial core, as predicted by tilted axis cranking calculations.

DOI: 10.1103/PhysRevC.69.024317 PACS number(s): 21.10.Re, 23.20.En, 23.20.Lv, 27.60.+j

I. INTRODUCTION

In the $A \approx 100$ mass region, nuclei with $40 \leqslant Z \leqslant 50$ have exhibited several shape transitions. Different types of deformation (prolate, oblate, and triaxial) are observed and can coexist in the same nucleus, where the equilibrium deformation will depend on the interplay of the driving forces when two or more high-*j* quasiparticles are involved. In this region, bands formed by one $g_{9/2}$ quasiproton in odd Rh [1,2] and Ag [3–6] isotopes, with the proton Fermi level in the upper half of the $g_{9/2}$ subshell, present a large signature splitting ($\sim$200 keV). When two quasineutrons of the $h_{11/2}$ orbital are coupled to the $\pi g_{9/2}$ configuration, the signature splitting becomes small or disappears entirely and the $B(M1)/B(E2)$ ratios become relatively large. These characteristics indicate a transition from the triaxial $\gamma \approx -30°$ (in the Lund convention) to prolate collective shape $\gamma \approx 0°$ [7]. In this mass region, another type of band with these characteristics has been attributed to large values of *K*. Bands based on the $(g_{9/2})^2$ configuration, eventually with additional quasiparticles, could present $K \approx 8$, as observed in the neighboring nuclei [1,3,8,9].

The ^{105}Rh nucleus is situated on the neutron-rich side of the stability line. Its population via a fusion evaporation reaction is hindered by a lack of suitable target-projectile combinations. In this work, we present the results of an investigation of ^{105}Rh with the ^{100}Mo(^{11}B, $\alpha 2n\gamma$) reaction. Previous to the present work, only four bands were known [2]. Several new structures with rotational characteristics were identified. In particular, high-spin members of a rotational band built on the intruder orbital $1/2^+$[431] have been identified for the first time in this nucleus. Moreover, a pair of structures, previously unknown, are suggested to be chiral partners [10]. This type of band is predicted by the tilted axis cranking (TAC) model [10,11] and was first identified experimentally in the odd-odd nuclei of the $A \sim 130$ region [12–15]. It is generated by a combination of geometry and dynamics, with particle, hole, and collective angular momenta each aligning along a different principal axis of the triaxial deformation of the core, breaking chiral symmetry in the intrinsic system. In this mass region, the roles of particles and holes are played by the valence $h_{11/2}$ neutrons and $g_{9/2}$ protons, respectively.

II. EXPERIMENTAL PROCEDURES

The high-spin states in the ^{105}Rh nucleus have been populated by the ^{100}Mo(^{11}B, $\alpha 2n\gamma$) reaction at 43 MeV beam energy. The beam was provided by the Pelletron Tandem Accelerator of the University of São Paulo. The target used was an $\approx$18 mg/cm^2 metallic self-supporting foil of enriched ^{100}Mo sufficiently thick in order to stop the recoils. γ rays and charged particles have been detected using the SACI-PERERE array. SACI [16] (*Sistema Ancilar de Cintiladores*) is a 4π-charged-particle telescope system consisting of 11 plastic phoswich scintillators, disposed in the geometry of a dodecahedron. Each telescope consists of a 0.1 mm thick fast scintillation (BC400, 2.4 ns) ΔE detector bonded to a 10 mm thick long decay time (BC444, 264 ns) *E* detector. The light-charged-particle detector array (SACI) enabled the selection of the evaporated charged particle fold in coincidence with the observed γ rays. PERERE [17] (*Pequeno Espectrômetro de Radiação Eletromagnética com Rejeição de Espalhamento*) is the γ-ray spectrometer consisting of 4 HpGe detectors with BGO Compton shields (two detectors were

*Present address: IAC, Idaho State University, Pocatello, ID 83209.

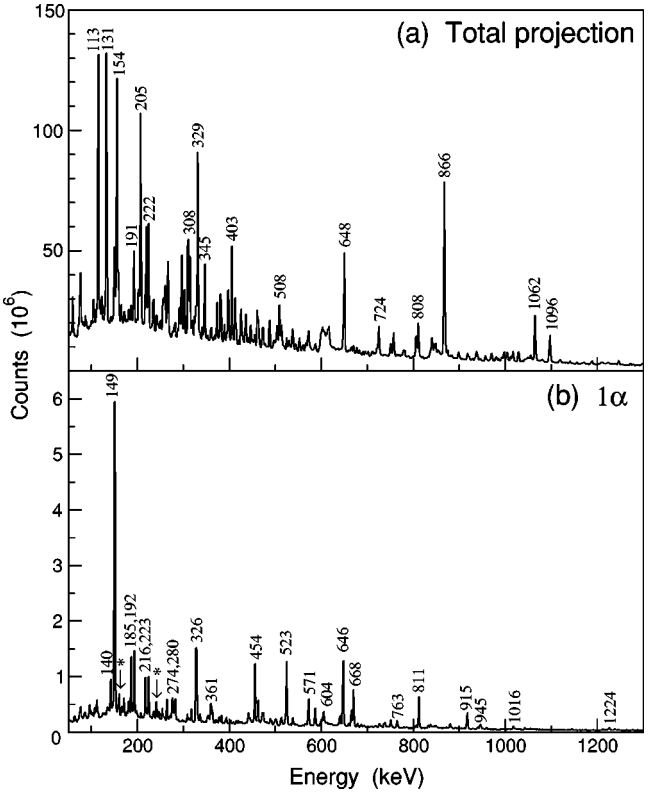

FIG. 1. γ-ray spectra (a) total projection and (b) gated with particle fold 1α. In (a) most lines are from ^{107,108}Ag and in (b) from ^{105}Rh. The transitions marked with asterisks belong to ^{104}Rh.

Ortec GMX of about 20% efficiency and the other two were Canberra REGe of 60% efficiency). Two of these detectors were placed at 37° and the other two at 101° with respect to the beam direction. The total photopeak efficiency (around 1.3 MeV) of the system is about 0.5%. Events were collected on tape when at least two HPGe detectors fired in coincidence. The data were taken for a period of 136 h. A total of 85×10^6 Compton-suppressed events was collected. The data have been sorted into symmetrized total γ-γ, α-gated, and p-gated γ-γ matrices with 1.7×10^8, 2.5×10^6, and 2.7×10^6 counts, respectively. The data were analyzed using the VPAK [18] and RADWARE [19] spectrum analysis codes.

The main exit channels of the reaction are the evaporation of three and four neutrons leading to Ag isotopes [2,3,8]. Some amount of incomplete fusion appears to have enhanced the $\alpha 2n$ channel, as compared to PACE code fusion-evaporation predictions. The γ-ray transitions belonging to ^{105}Rh were identified by setting gates on charged particle fold 1α (see Fig. 1). γ rays from ^{104}Rh (corresponding to $1\alpha 3n$ reaction), which is the main contaminant channel in the 1α-gated spectra, were identified from previous work [20]. The assignment of the spins and parities to the ^{105}Rh levels was based on the DCO (directional correlation from oriented states) ratios. A γ-γ matrix was constructed by sorting the data from the two detectors positioned at 37° against the two detectors at 101° with respect to the beam direction. Gates were set on each axis on several strong quadrupole transitions and the intensity of other transitions observed in the two spectra has been extracted. $I_\gamma(37°)$ and $I_\gamma(101°)$ represent the intensity of a transition when gating on the 101° and 37° detector axes, respectively. The theoretical DCO ratios

$$R_{\mathrm{DCO}} = \frac{I_\gamma(37°)}{I_\gamma(101°)},$$

which are obtained for the present geometry and reaction, are $R_{\mathrm{DCO}}=1.0$ for quadrupole transitions and $R_{\mathrm{DCO}}=0.49$ for pure dipole transitions ($\Delta I=1$), with intermediate values for moderate positive mixing ratios (δ). It should be noted that $\Delta I=0$ transitions could give DCO ratios between 1.1 (the value for a pure dipole) and 0.44 (for large mixing ratios). In some cases it was only possible to set an adequate gate on a previously determined dipole transition (mixed or not). In such cases the resulting DCO has to be multiplied by the DCO of the gating transition in order to obtain the value corresponding to that of a quadrupole gate for uniformity.

The stopping time of the recoils in the Mo target is estimated to be about 0.6 ps. Since no significant Doppler broadening was observed in any of the γ-ray lines assigned to ^{105}Rh, it can be inferred that their effective lifetimes are at least a fraction of that time.

III. RESULTS

The level scheme of ^{105}Rh deduced from the present work, based on the coincidence relationships, intensity balances on each level and energy sums from different paths using the 1α-gated matrix, is shown in Fig. 2 and is essentially in agreement with previous work [2]. The γ-ray energies and relative intensities of all the transitions assigned to ^{105}Rh are given in Table I, which also shows the DCO ratios and the resulting spin and parity assignments. These assignments are, however, all based on the assumption that the spin (parity) of the ground state (previously known) is $7/2^+$. The assignments without parentheses are, therefore, to be regarded as certain, from the DCO results and internal consistency arguments, relative to the spin of that state. The observed levels are grouped into eight structures with rotational characteristics, labeled 1–8 in Fig. 2 for the purposes of discussion, four of which (4, 6, 7, and 8) were observed for the first time.

Band 1 is the yrast band with the $7/2^+$ ground state as the bandhead and presents, in the positive signature component, slightly stronger $E2$ crossovers than $M1$ transitions. In the present measurement, band 1 was observed up to spin $I^\pi=(29/2^+)$. Band 2 is characterized by strong $M1$ transitions and weak $E2$ crossovers. The spin for the lowest level assigned to $23/2^+$ in band 2 was based on the DCO ratios of the 460 and 738 keV transitions. This level had been assigned to $21/2^+$ in the previous work [2]. This structure is thus assigned a bandhead $I^\pi=23/2^+$ and was extended by two new transitions up to $I^\pi=(33/2^+)$ in the present work.

In band 3 we have, for the first time, observed transitions from the $7/2^-$ and $11/2^-$ unfavored states. This band is characterized by strong $E2$ and very weak $M1$ transitions in the positive signature component. At relatively higher energies

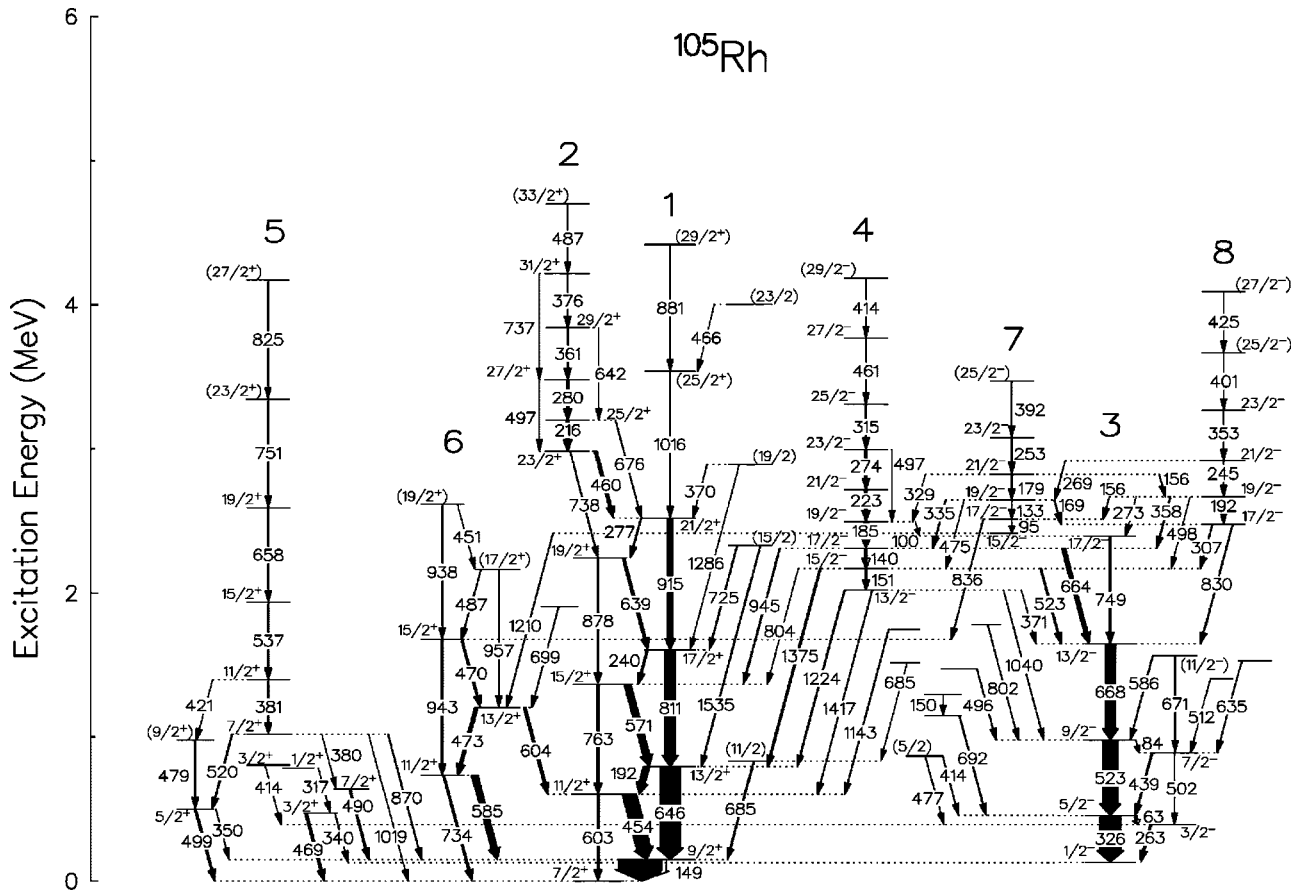

FIG. 2. The level scheme of ^{105}Rh. The energies of the transitions are given in keV. The filled width of the arrows is proportional to the relative γ-ray intensity.

and spins, three magnetic dipole bands (labeled 4, 7, and 8) were observed. These bands present similar characteristics: strong $M1$ transitions and weak or unobserved $E2$ crossovers and are very regular in energy spacing. Figure 3 shows a sum of clean double gates for the negative parity bands labeled 7 and 8.

In Fig. 2, band 5, composed of $E2$ transitions, is shown as built on the $I^{\pi}=7/2^{+}$ level at around 1 MeV excitation energy. However, two γ transitions of 414 and 317 keV observed in this work have been assigned to the decay of the $I^{\pi}=3/2^{+}$ and $I^{\pi}=1/2^{+}$ levels at 806 and 787 keV excitation energies, respectively. We identify these two levels as the lowest members of the multiplet of states with $1/2^{+}$ to $9/2^{+}$ spins, first populated by means of $(^{3}\mathrm{He},d)$ stripping reactions by Rogowski *et al.* [21] in ^{105}Rh, and assigned to the $\pi 1/2^{+}[431]$ configuration from the $(g_{7/2},d_{5/2})$ intruder orbital. A new structure (labeled 6) has been observed in the present work with characteristics very similar to those observed in ^{107,111}Rh [22,23]. The bandhead is the low lying second $I^{\pi}=11/2^{+}$ state. Both $M1$ and crossover $E2$ transitions are observed, with linking transitions to the yrast band. The negative signature is energetically favored. Figure 4 shows a sum of clean double gates for the positive parity bands labeled 5 and 6.

Besides showing new bands, the current data extend to higher spins than those observed in previous work [2]. There are no major disagreements between these two works, except for the placement of two transitions and the spin assignment of band 2. Our data do not confirm the existence of the 481 keV transition, but, instead, two new γ rays of 376 and 487 keV were placed at the top of band 2. Also the 426 keV transition placed in band 3 was not observed. The two new states observed in the present work, with $I^{\pi}=7/2^{-}$ and $I^{\pi}=11/2^{-}$, have been assigned to the unfavored signature of band 3.

The establishment of negative parity for bands 4, 7, and 8 has been accomplished in two steps: first, the spins are assigned from the consistency with the DCO measurements and previously known assignments of lower lying levels [2]; second, the branching quadrupole transitions are assumed to be $E2$, since $M2$ transitions are very retarded and should be at least two or three orders of magnitude weaker than in-band or relatively high energy dipole transitions from the same level. In the case of band 4, the DCO of the 664 keV transition (towards the previously known $13/2^{-}$ state of band 3) corresponds to that of a quadrupole. The experimental lower limit for the lifetime of an $M2$ transition of that energy in this mass region is about 11 ns. Together with the existence of the 945 keV transition from the same state of band 4 towards the $15/2^{+}$state of band 1, consistency can only be achieved with a spin of 17/2 and with negative parity for the state of 2310.7 keV of band 4, which also decays by the in-band 140 keV dipole transition. Bands 7 and 8 can be established relative to band 4, both decaying by dipole tran-

TABLE I. γ-ray energy, initial and final excitation energies, spin and parity assignments, relative intensity, and DCO ratio for the transitions in ^{105}Rh. The relative intensities (normalized to 100 for the 453.7 keV transition) were obtained from the analysis of the 1α-gated matrix.

E_γ (keV)	E_i (keV)	E_f (keV)	$I_i^\pi \rightarrow I_f^\pi$	I_γ	DCO ratio
63.4(2)	456.2	392.8	$5/2^- \rightarrow 3/2^-$	8.5(9)	0.83(30)
84.4(1)	979.0	894.8	$9/2^- \rightarrow 7/2^-$	0.61(21)	
95.3(2)	2512.6	2417.3	$17/2^- \rightarrow 15/2^-$	1.43(18)	
100.2(2)	2496.0	2396.2	$19/2^- \rightarrow 17/2^-$	0.76(12)	
133.0(2)	2645.7	2512.6	$19/2^- \rightarrow 17/2^-$	1.89(21)	0.34(20)
140.4(1)	2310.7	2170.3	$17/2^- \rightarrow 15/2^-$	17.1(9)	0.71(14)
149.2(1)	149.2	0.0	$9/2^+ \rightarrow 7/2^+$	$>282(8)$[a]	0.74(16)
149.5(4)	1297.7	1147.7		1.22(37)	
151.1(1)	2170.3	2019.2	$15/2^- \rightarrow 13/2^-$	8.8(6)	0.76(22)
156.0(1)	2825.1	2669.1	$21/2^- \rightarrow 19/2^-$	1.98(18)	0.34(20)
156.4(1)	2669.1	2512.6	$19/2^- \rightarrow 17/2^-$	0.88(24)	
168.6(1)	2645.7	2477.1	$19/2^- \rightarrow 17/2^-$	3.32(24)	0.63(25)
179.4(1)	2825.1	2645.7	$21/2^- \rightarrow 19/2^-$	5.79(37)	0.55(27)
185.3(1)	2496.0	2310.7	$19/2^- \rightarrow 17/2^-$	29.3(15)	0.68(9)
191.9(1)	2669.1	2477.1	$19/2^- \rightarrow 17/2^-$	3.95(34)	0.49(16)
192.2(1)	795.0	602.8	$13/2^+ \rightarrow 11/2^+$	41.8(21)	0.78(11)
216.0(1)	3197.6	2981.6	$25/2^+ \rightarrow 23/2^+$	16.5(9)	0.52(8)
222.7(1)	2718.7	2496.0	$21/2^- \rightarrow 19/2^-$	20.1(11)	0.65(11)
239.7(1)	1605.6	1366.0	$17/2^+ \rightarrow 15/2^+$	12.2(7)	0.62(15)
245.2(1)	2914.4	2669.1	$21/2^- \rightarrow 19/2^-$	2.90(24)	0.69(23)
252.8(1)	3078.0	2825.1	$23/2^- \rightarrow 21/2^-$	4.42(34)	0.61(26)
263.0(1)	392.8	129.8	$3/2^- \rightarrow 1/2^-$	$>12.9(11)$[a]	0.55(10)
268.7(1)	2914.4	2645.7	$21/2^- \rightarrow 19/2^-$	2.44(21)	
273.0(2)	2669.1	2396.2	$19/2^- \rightarrow 17/2^-$	1.43(21)	
274.4(1)	2993.1	2718.7	$23/2^- \rightarrow 21/2^-$	12.7(7)	0.68(13)
277.0(1)	2521.1	2244.2	$21/2^+ \rightarrow 19/2^+$	5.7(4)	0.49(20)
280.4(2)	3478.1	3197.6	$27/2^+ \rightarrow 25/2^+$	14.8(8)	0.60(12)
306.8(1)	2477.1	2170.3	$17/2^- \rightarrow 15/2^-$	3.81(34)	0.55(32)
315.4(1)	3308.5	2993.1	$25/2^- \rightarrow 23/2^-$	6.83(43)	0.61(14)
316.6(4)	786.9	470.0	$1/2^+ \rightarrow 3/2^+$	0.79(37)	
326.4(1)	456.2	129.8	$5/2^- \rightarrow 1/2^-$	146(17)	1.05(7)
329.4(2)	2825.1	2496.0	$21/2^- \rightarrow 19/2^-$	1.37(18)	0.70(37)
335.0(1)	2645.7	2310.7	$19/2^- \rightarrow 17/2^-$	4.79(37)	0.46(13)
340.2(4)	470.0	129.8	$3/2^+ \rightarrow 1/2^-$	1.4(7)	
350.4(3)	499.5	149.2	$5/2^+ \rightarrow 9/2^+$	2.0(5)	
352.8(1)	3267.2	2914.4	$23/2^- \rightarrow 21/2^-$	3.32(27)	0.56(15)
358.4(1)	2669.1	2310.7	$19/2^- \rightarrow 17/2^-$	4.9(4)	0.46(25)
361.3(1)	3839.4	3478.1	$29/2^+ \rightarrow 27/2^+$	8.35(46)	0.47(12)
369.6(2)	2890.8	2521.1	$(19/2) \rightarrow 21/2^+$	1.55(27)	0.71(28)
371.2(6)	2019.2	1647.1	$13/2^- \rightarrow 13/2^-$	0.64(30)	
376.1(1)	4215.5	3839.4	$31/2^+ \rightarrow 29/2^+$	3.78(27)	0.48(15)
380.3(6)	1019.0	638.8	$7/2^+ \rightarrow 7/2^+$	0.67(12)	
380.8(1)	1399.8	1019.0	$11/2^+ \rightarrow 7/2^+$	8.6(7)	1.14(28)
392.0(1)	3469.9	3077.9	$(25/2^-) \rightarrow 23/2^-$	2.04(21)	0.78(45)
400.6(2)	3667.7	3267.2	$(25/2^-) \rightarrow 23/2^-$	1.22(15)	
413.5(3)	806.0	392.8	$3/2^+ \rightarrow 3/2^-$	0.79(27)	

TABLE I. (*Continued.*)

E_γ (keV)	E_i (keV)	E_f (keV)	$I_i^\pi \rightarrow I_f^\pi$	I_γ	DCO ratio
413.7(4)	869.8	456.2	$(5/2) \rightarrow 5/2^-$	2.6(6)	
414.3(2)	4183.6	3769.3	$(29/2^-) \rightarrow 27/2^-$	1.28(12)	
421.1(3)	1399.8	978.5	$11/2^+ \rightarrow (9/2^+)$	1.07(18)	
424.8(2)	4092.5	3667.7	$(27/2^-) \rightarrow (25/2^-)$	0.76(12)	
438.6(1)	894.8	456.2	$7/2^- \rightarrow 5/2^-$	9.1(8)	0.53(12)
451.2(4)	2615.3	2164.0	$(19/2^+) \rightarrow (17/2^+)$	1.28(30)	
453.7(1)	602.8	149.2	$11/2^+ \rightarrow 9/2^+$	100(5)	0.69(13)
460.4(2)	2981.6	2521.1	$23/2^+ \rightarrow 21/2^+$	19.9(12)	0.58(12)
460.8(1)	3769.3	3308.5	$27/2^- \rightarrow 25/2^-$	3.11(24)	0.52(16)
465.6(3)	4002.4	3536.8	$(23/2) \rightarrow (25/2^+)$	1.04(23)	0.49(22)
469.4(6)	470.0	0.0	$3/2^+ \rightarrow 7/2^+$	14.63(37)	
469.9(1)	1676.9	1206.9	$15/2^+ \rightarrow 13/2^+$	10.6(8)	0.52(17)
472.5(2)	1206.9	734.3	$13/2^+ \rightarrow 11/2^+$	22.3(14)	0.59(22)
475.5(17)	2645.7	2170.3	$19/2^- \rightarrow 15/2^-$	1.37(27)	
476.7(2)	869.8	392.8	$(5/2) \rightarrow 3/2^-$	2.23(36)	0.65(17)
479.0(1)	978.5	499.5	$(9/2^+) \rightarrow 5/2^+$	5.2(7)	1.28(48)
486.8(2)	4702.3	4215.5	$(33/2^+) \rightarrow 31/2^+$	1.62(18)	
487.0(2)	2164.0	1676.9	$(17/2^+) \rightarrow 15/2^+$	2.65(37)	0.63(33)
489.6(1)	638.8	149.2	$7/2^+ \rightarrow 9/2^+$	10.7(9)	0.62(33)
496.2(2)	1475.2	979.0	$\rightarrow 9/2^-$	2.9(5)	
496.5(8)	3478.1	2981.6	$27/2^+ \rightarrow 23/2^+$	0.91(21)	
496.8(13)	2993.1	2496.0	$23/2^- \rightarrow 19/2^-$	0.61(27)	
498.3(4)	2669.1	2170.3	$19/2^- \rightarrow 15/2^-$	1.22(34)	
499.4(2)	499.5	0.0	$5/2^+ \rightarrow 7/2^+$	11.59(34)	1.04(27)
502.0(2)	894.8	392.8	$7/2^- \rightarrow 3/2^-$	1.68(30)	0.88(26)
511.5(2)	1406.3	894.8	$\rightarrow 7/2^-$	2.16(37)	
519.6(1)	1019.0	499.5	$7/2^+ \rightarrow 5/2^+$	7.0(8)	0.71(16)
522.8(1)	979.0	456.2	$9/2^- \rightarrow 5/2^-$	108(6)	0.97(7)
522.9(1)	2170.3	1647.1	$15/2^- \rightarrow 13/2^-$	8.4(6)	
536.9(1)	1936.7	1399.8	$15/2^+ \rightarrow 11/2^+$	8.7(7)	1.18(20)
570.9(1)	1366.0	795.0	$15/2^+ \rightarrow 13/2^+$	47.9(27)	0.80(16)
585.1(1)	734.3	149.2	$11/2^+ \rightarrow 9/2^+$	43.3(24)	0.48(20)
586.4(2)	1565.5	979.0	$(11/2^-) \rightarrow 9/2^-$	4.2(6)	0.86(30)
602.7(1)	602.8	0.0	$11/2^+ \rightarrow 7/2^+$	13.7(13)	0.90(19)
604.1(1)	1206.9	602.8	$13/2^+ \rightarrow 11/2^+$	17.3(11)	0.87(21)
635.2(2)	1530.0	894.8	$\rightarrow 7/2^-$	2.56(43)	
638.7(1)	2244.2	1605.6	$19/2^+ \rightarrow 17/2^+$	17.1(11)	0.83(17)
642.0(5)	3839.4	3197.6	$29/2^+ \rightarrow 25/2^+$	1.07(21)	
645.8(1)	795.0	149.2	$13/2^+ \rightarrow 9/2^+$	146(7)	0.98(10)
657.4(2)	2594.2	1936.7	$19/2^+ \rightarrow 15/2^+$	3.63(37)	0.88(27)
663.6(1)	2310.7	1647.1	$17/2^- \rightarrow 13/2^-$	26.9(15)	0.99(12)
668.1(1)	1647.1	979.0	$13/2^- \rightarrow 9/2^-$	73.2(40)	1.01(9)
670.9(3)	1565.5	894.8	$(11/2^-) \rightarrow 7/2^-$	1.9(4)	
676.4(2)	3197.6	2521.1	$25/2^+ \rightarrow 21/2^+$	3.8(4)	1.04(35)
684.5(2)	833.7	149.2	$(11/2) \rightarrow 9/2^+$	7.5(9)	0.81(24)
685.4(6)	1519.2	833.7	$\rightarrow (11/2)$	0.76(30)	
691.5(2)	1147.7	456.2	$\rightarrow 5/2^-$	4.5(7)	0.85(27)

TABLE I. (*Continued.*)

E_γ (keV)	E_i (keV)	E_f (keV)	$I_i^\pi \rightarrow I_f^\pi$	I_γ	DCO ratio
698.8(3)	1905.7	1206.9	$\rightarrow 13/2^+$	2.65(43)	
724.7(2)	2330.1	1605.6	$(15/2) \rightarrow 17/2^+$	5.1(6)	
734.3(1)	734.3	0.0	$11/2^+ \rightarrow 7/2^+$	20.1(18)	0.67(26)
736.9(6)	4215.5	3478.1	$31/2^+ \rightarrow 27/2^+$	1.28(37)	
737.5(2)	2981.6	2244.2	$23/2^+ \rightarrow 19/2^+$	4.42(43)	0.94(29)
749.1(1)	2396.2	1647.1	$17/2^- \rightarrow 13/2^-$	13.5(9)	1.01(19)
750.6(2)	3344.7	2594.2	$(23/2^+) \rightarrow 19/2^+$	1.80(27)	0.82(30)
763.2(1)	1366.0	602.8	$15/2^+ \rightarrow 11/2^+$	17.2(11)	0.88(22)
802.0(3)	1781.0	979.0	$\rightarrow 9/2^-$	2.01(46)	1.04(43)
803.8(4)	2170.3	1366.0	$15/2^- \rightarrow 15/2^+$	1.37(27)	0.84(50)
810.6(5)	1605.6	795.0	$17/2^+ \rightarrow 13/2^+$	74.7(40)	1.00(11)
825.2(6)	4169.9	3344.7	$(27/2^+) \rightarrow (23/2^+)$	0.76(18)	
830.0(1)	2477.1	1647.1	$17/2^- \rightarrow 13/2^-$	4.82(46)	0.85(25)
835.6(2)	2512.6	1676.9	$17/2^- \rightarrow 15/2^+$	2.84(45)	
869.9(1)	1019.0	149.2	$7/2^+ \rightarrow 9/2^+$	4.4(6)	0.31(20)
878.2(1)	2244.2	1366.0	$19/2^+ \rightarrow 15/2^+$	9.7(7)	0.88(25)
880.6(11)	4417.4	3536.8	$(29/2^+) \rightarrow (25/2^+)$	1.07(37)	0.87(38)
915.4(6)	2521.1	1605.6	$21/2^+ \rightarrow 17/2^+$	34.2(21)	0.97(12)
938.4(2)	2615.3	1676.9	$(19/2^+) \rightarrow 15/2^+$	2.96(46)	
942.8(1)	1676.9	734.3	$15/2^+ \rightarrow 11/2^+$	10.6(10)	0.89(43)
944.8(1)	2310.7	1366.0	$17/2^- \rightarrow 15/2^+$	6.25(46)	0.52(21)
957.1(2)	2164.0	1206.9	$(17/2^+) \rightarrow 13/2^+$	4.4(5)	
1015.7(2)	3536.8	2521.1	$(25/2^+) \rightarrow 21/2^+$	3.9(5)	1.13(42)
1019.0(4)	1019.0	0.0	$7/2^+ \rightarrow 7/2^+$	2.4(6)	1.7(9)
1040.4(3)	2019.2	979.0	$13/2^- \rightarrow 9/2^-$	1.74(24)	
1142.5(2)	1745.3	602.8	$\rightarrow 11/2^+$	3.9(6)	0.81(35)
1210.4(2)	2417.3	1206.9	$15/2^- \rightarrow 13/2^+$	2.9(5)	
1224.3(1)	2019.2	795.0	$13/2^- \rightarrow 13/2^+$	6.4(6)	1.08(48)
1285.6(5)	2890.8	1605.6	$(19/2) \rightarrow 17/2^+$	1.22(37)	1.08(39)
1375.2(1)	2170.3	795.0	$15/2^- \rightarrow 13/2^+$	11.0(8)	0.37(15)
1416.6(2)	2019.2	602.8	$13/2^- \rightarrow 11/2^+$	3.1(4)	0.35(15)
1534.8(2)	2330.1	795.0	$(15/2) \rightarrow 13/2^+$	5.1(6)	0.39(21)

[a]Sum of the intensities of the feeding transitions divided by the conversion coefficient factor $(1+\alpha)$ of the decaying transition from the same level.

sitions (from the DCO) from the $19/2^-$ states by the 335 and 358 keV transitions, respectively, to the $17/2^-$ state of band 4, and by the transitions of 476 and 498 keV, respectively, to the $15/2^-$ state of band 4, with intensities comparable to the dipole branchings from the same levels. For the 95 keV transition (the lowest of band 7), although no DCO result is available, a similar argument excludes also the possibility of $E1$ or $E2$ multipolarity, since the experimental lower limit of the lifetime for this mass region of an electric dipole or quadrupole transition of 95 keV is about 35 ps and 8 ns, respectively. In those cases the transition would not be expected to compete with a high energy $E1$ transition (836 keV) from the same level, which is only about two times faster (from the experimental branching ratio). The chances of the 95 keV transition being other than an in-band $M1$ are therefore very small. The cross-talking dipole transitions of relatively low energies between the bands are also consistent with a common parity assignment.

IV. DISCUSSION

The experimental Routhians e' and alignments i_x shown in Fig. 5 as a function of rotational frequency $\hbar\omega$ were calculated according to the standard procedure described in Refs. [25,26], with the Harris parametrization of the moment of inertia, $\mathcal{J}_0 = 4\hbar^2$ MeV^{-1} and $\mathcal{J}_1 = 40\hbar^4$ MeV^{-3}, taken from ^{102}Ru [27]. The quasiparticle Routhians based on a deformed Woods-Saxon potential including pairing interaction [28], calculated for $Z=45$ and $N=60$, are shown in Fig. 6. The deformation ($\beta_2 = 0.19, \beta_4 = 0.0, \gamma = -30°$) and pairing-gap pa-

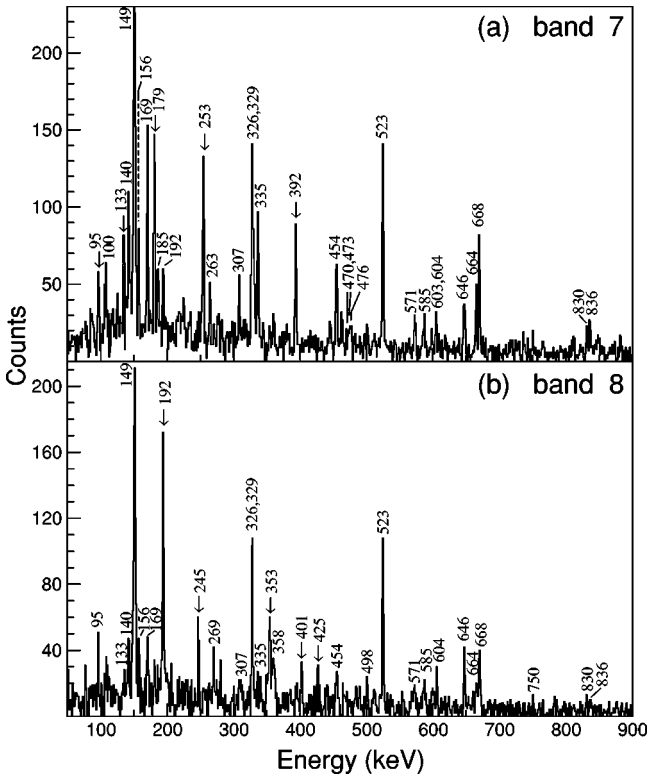

FIG. 3. γ-ray spectra from the 1α-gated matrix. Sum of gates on (a) 179, 253, and 392 keV transitions belonging to band 7 and (b) 245, 307, and 353 keV transitions belonging to band 8, in ^{105}Rh.

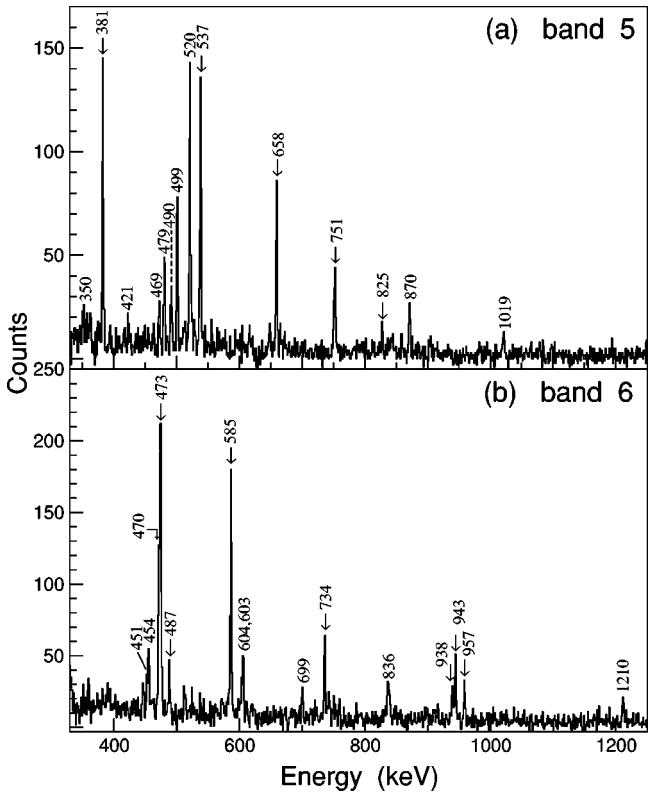

FIG. 4. γ-ray spectra from the 1α-gated matrix. Sum of gates on (a) 499, 381, and 537 keV transitions belonging to band 5 and (b) 470, 473, and 585 keV transitions belonging to band 6, in ^{105}Rh.

rameters used were chosen in accordance with the total Routhian surface (TRS) calculations [28,29] for the $\pi g_{9/2}$ configuration (see also Fig. 7). The lowest quasiproton energy levels of the positive parity are labeled *A*, *B*, *C*, and *D*; and those of negative parity (1/2[301]), *E* and *F*. For the neutrons, the first available $h_{11/2}$ orbitals are *e*, *f*, *g*, and *h* and for $(g_{7/2},d_{5/2})$, *a*, *b*, *c*, and *d*, respectively.

A. The positive parity bands

In the present measurement, band 1 based on $\pi g_{9/2}$ (yrast up to spin $I=21/2$) was observed up to $I^{\pi}=(29/2^{+})$. The aligned angular momentum is $\sim 3\hbar$ and the signature splitting is large, $\Delta e' \approx 200$ keV. Yrast bands with $g_{9/2}$ configuration have been observed in odd-*Z* nuclei in this mass region [1,3–5,22,23]. Band 2 presents a gain in alignment of

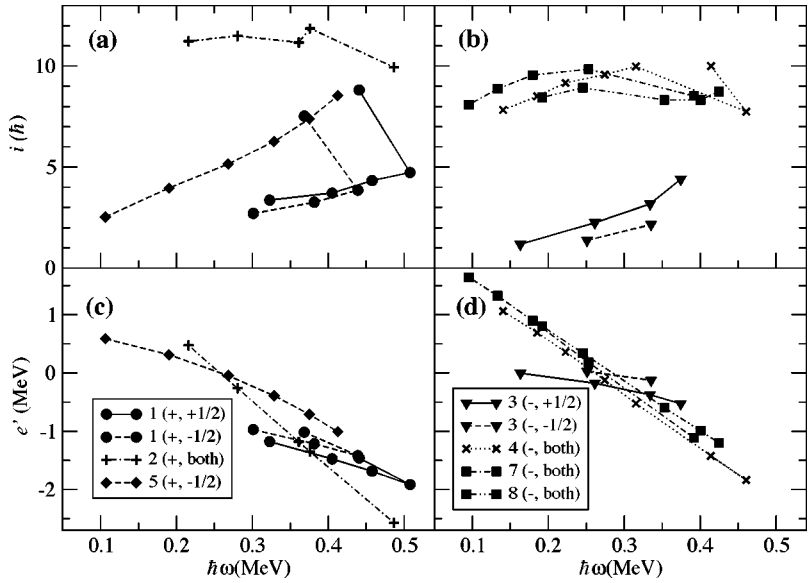

FIG. 5. Experimental quasiparticle (a), (b) alignments and (c), (d) Routhians as a function of the rotational frequency $\hbar\omega$ for the rotational bands in ^{105}Rh. The symbols correspond to the numbering of the bands and parity, signature (π,α) as indicated in the bottom panels.

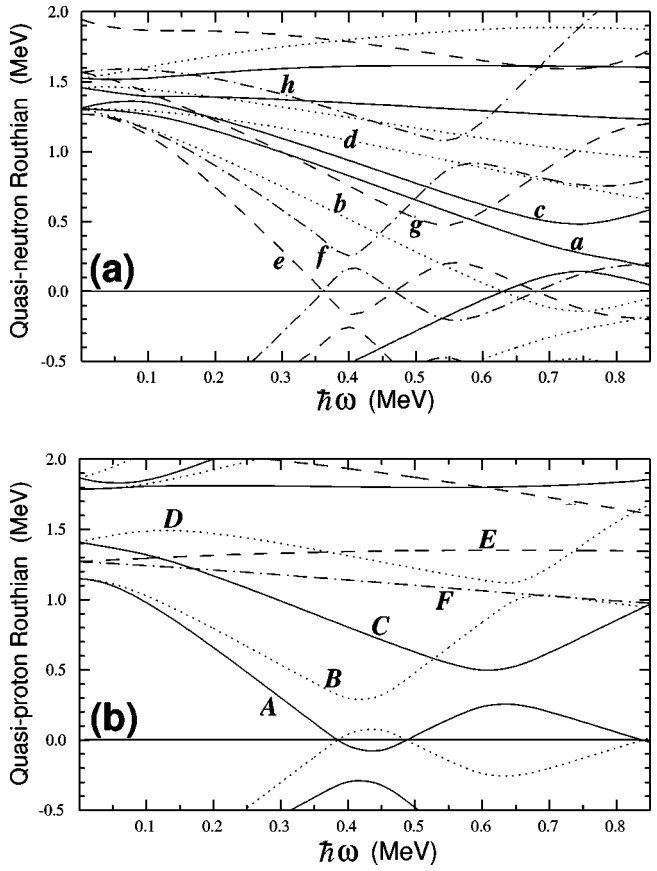

FIG. 6. Quasiparticle Routhians as a function of the rotational frequency $\hbar\omega$ for (a) neutrons and (b) protons. Calculated at $\beta_2=0.19$, $\beta_4=0$, and $\gamma=-30°$ in ^{105}Rh. The following convention is used for the levels: solid lines ($\pi=+,\alpha=+1/2$), dotted line ($\pi=+,\alpha=-1/2$), dot-dashed line ($\pi=-,\alpha=+1/2$), and dashed line ($\pi=-,\alpha=-1/2$). The configurations are labeled by letters.

$\sim 10\hbar$ with relation to band 1, corresponding to the alignment of the first two $h_{11/2}$ quasineutrons (ef). The two bands cross at a frequency of ≈ 0.4 MeV, as expected.

Bands similar in structure to band 5 (see Fig. 2) are known in other Rh and Ag isotopes. We were able to observe only the negative signature of this structure, up to spin $(27/2)$. The level assigned to $3/2^+$ at 806 keV is believed to be the lowest level with negative signature, in spite of the nonobservation of the $7/2^+ \rightarrow 3/2^+$ transition. The $1/2^+$ level, just below this $3/2^+$ state, which decays by the 317 keV transition, could be the lowest level belonging to the other signature. As mentioned earlier, the $1/2^+$, $3/2^+$, $5/2^+$, $7/2^+$, and $9/2^+$ states were identified previously using the ^{104}Ru$(^3$He$,d)^{105}$Rh reaction by Rogowski *et al.* [21]. Kaffrel *et al.* have also observed this rotational-like sequence in ^{107,109}Rh [30,31] and have proposed the $\pi\ 1/2^+[431]$ configuration, originating from the $\pi(g_{7/2},d_{5/2})$ subshell, located above the $Z=50$ major shell gap. This orbital has a large deformation and tends towards well-elongated shapes ($\beta \sim 0.3$), based on the best fits of the experimental levels to rotor plus quasiparticle calculations [21,22,30,31]. In fact, CSM calculations also show that with $\beta \approx 0.25$, the intruder $1/2^+[431]$ proton orbital tends towards a lower excitation

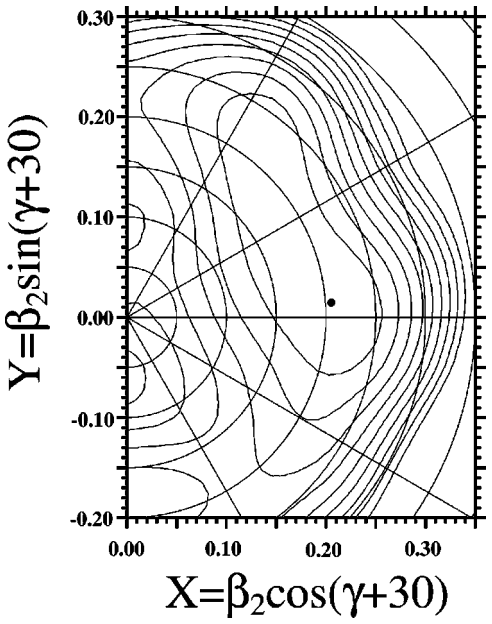

FIG. 7. Total Routhian surface calculations for the Afb configuration at $\hbar\omega=0.190$ MeV in ^{105}Rh. The thick dot indicates the position of the equilibrium deformation.

energy for an axially symmetric shape. It is interesting to note also that according to Rogowski *et al.* [32], the excitation energies of the deformed bands show a minimum exactly at $N=66$ neutron midshell for Ag isotopes, but shifts to $N=64$ for Rh isotopes [33].

The band labeled 6 in Fig. 2 was observed for the first time. Very similar bands have also been observed in the $A=107-113$ odd Rh isotopes by Venkova *et al.* [22,23] and, with the help of a triaxial rotor plus quasiparticles model, were identified as the γ-vibrational band, formed by the coupling of the $7/2^+[413]$ proton state $(\pi g_{9/2})$ to the $K^\pi=2^+$ γ vibration of the core. Those authors claim that the occurrence of those sidebands deexciting towards the main $\pi g_{9/2}$ excitations is evidence for the deviation from axial symmetry. The systematics of the ratio of the second to the first I^π

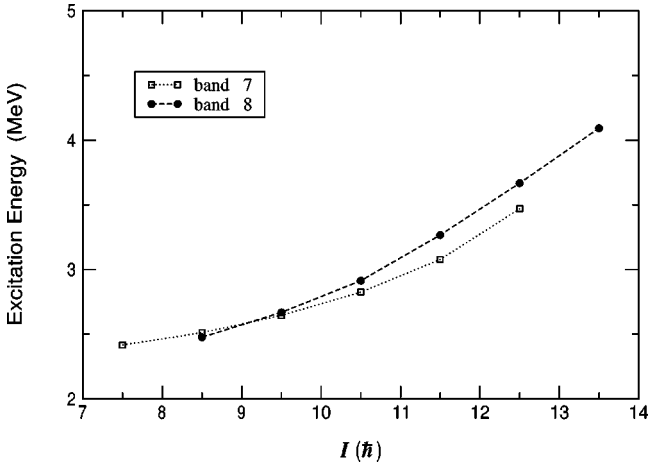

FIG. 8. Experimental excitation energy as a function of angular momentum for bands 7 and 8 in ^{105}Rh.

$=11/2^+$ states in those odd Rh isotopes (including ^{105}Rh), all between 1.2 and 1.3, is compelling evidence for a common underlying nature for all those bands. In even-even nuclei, the analogous ratio of the second to the first 2^+state was recognized by Davidov and Filippov [24] simply as a measure of the degree of triaxiality. This is also in agreement with our TRS calculations ($\beta=0.19,\gamma=-30°$). On the other hand, Venkova *et al.* [22] present the potential energy surface for the ground states of ^{105,107,109}Rh nuclei calculated using a microscopic self-consistent model [34]. According to these predictions, ^{105}Rh has a prolate shape in the ground state, in disagreement with the present conclusion. This illustrates the difficulty in producing precise theoretical predictions for this mass region.

B. The negative parity bands

In the present work we have observed both signature partners of the negative parity band labeled 3, assigned to the 1/2[301] configuration. We have also identified the transitions connecting the levels belonging to the two signature partners. This band presents an aligned angular momentum i_x of about $2\hbar$ and a large signature splitting ($\approx$200 keV) at 0.3 MeV, consistent with theoretical expectations.

Bands 4, 7, and 8 have similar characteristics, with strong $M1$ transitions and negligible signature splitting, band 4 being somewhat less excited. Bands 7 and 8 are nearly degenerate and present considerable cross-talk at low spin, which suggests a chiral doublet (Fig. 8) in a fashion similar to that observed in the $A\approx130$ mass region [12,13]. Two types of three quasiparticle negative parity configurations are available at low excitation energy: from $\pi1/2^-[301](g_{9/2})^2$ (with $K\approx8$) and $\pi g_{9/2}\otimes\nu h_{11/2}(g_{7/2},d_{5/2})$ parentage. Both types have been considered previously for band 4 in this nucleus [2] and for similar bands in neighboring nuclei, but we do not have a conclusive argument to distinguish between the two configurations from the present status of data and calculations. TRS predictions (see Fig. 7) show for the second configuration a very shallow minimum as a function of γ deformation. There is little variation in total Routhian in the interval from $-30°\leqslant\gamma\leqslant30°$. The position of the absolute minimum calculated depends on the particular combination of the signature of the quasiparticles involved in the configuration (A or B with e or f and a or b). The one shown in Fig. 7 corresponds to $\alpha=+1/2$ for which the absolute minimum is close to maximum triaxiality ($\gamma=-30°$). The TRS calculation, however, assumes a principal axis cranking rotation [35]. From a more general approach, considering a tilted axis rotation [36], one would expect that the combined polarization of $g_{9/2}$ proton hole, $h_{11/2}$ neutron particle, and the collective rotation could lead to a rather stabilized collective triaxial deformation ($\gamma=-30°$). This condition is suitable for the appearance of chirality in the intrinsic system, generating a pair of nearly degenerate bands. Hybrid TAC model [37] calculations were performed for ^{105}Rh which indeed present a chiral solution ($\varphi\neq0$ or 90°) for the $\pi g_{9/2}\otimes\nu h_{11/2}(g_{7/2},d_{5/2})$ basic configuration, assuming a triaxial shape with $\varepsilon_2=0.21,\gamma=30°$ (with pairing gaps $\Delta_p=0.97$ MeV and $\Delta_n=1.12$ MeV), but for an excited proton $g_{9/2}$ state, while the lowest state is planar (possibly corresponding to band 4). Table II presents the results for the tilting angles and total angular momentum as a function of rotational frequency. The total energy minimum as a function of the parameters is very shallow. Figure 9 presents the comparison of these results with the experimental values from bands 7 and 8. The agreement is reasonable, the theoretical values lying roughly in between the experimental values for the two bands due to the absence of tunneling (the chiral vibration [13]) in the model. In addition, the calculations reproduce the cross-talk between the bands at low spin. The experimental ratio of $B(M1)$ reduced transition probabilities between in-band and interband transitions is between 1.2 and 2.4 for the 21/2 and 19/2 states of both bands. The experimental lower limits of the $B(M1)/B(E2)$ (in-band) ratio for the 21/2 states of bands 7 and 8 are around $6\mu_N/e$ b; unfortunately, not very restrictive due to rather low statistics. The present version of the TAC code predicts $B(M1)/B(E2)\approx33\mu_N^2/e$ b for $J\approx9\hbar$, but does not allow for the disentanglement between in-band and interband transition intensities after chirality sets in. Chirality develops already at low spin which is unusual, and is probably related to the presence of a Fermi-aligned quasiparticle ($\nu g_{7/2}$), besides the particlelike and holelike excitations ($\nu h_{11/2}$ and $\pi g_{9/2}$, respectively).

TABLE II. Tilting angles (θ,φ) and angular momentum (J) as a function of rotational frequency $(\hbar\omega)$ from TAC calculations for the excited $\pi g_{9/2}\otimes\nu h_{11/2}g_{7/2}$ configuration in ^{105}Rh.

$\hbar\omega$ (MeV)	θ	φ	$J(\hbar)$
0.15	55°	0°	9.0
0.20	60°	23°	9.8
0.25	65°	38°	10.0
0.30	65°	43°	11.9
0.35	65°	48°	12.7
0.40	65°	54°	13.8

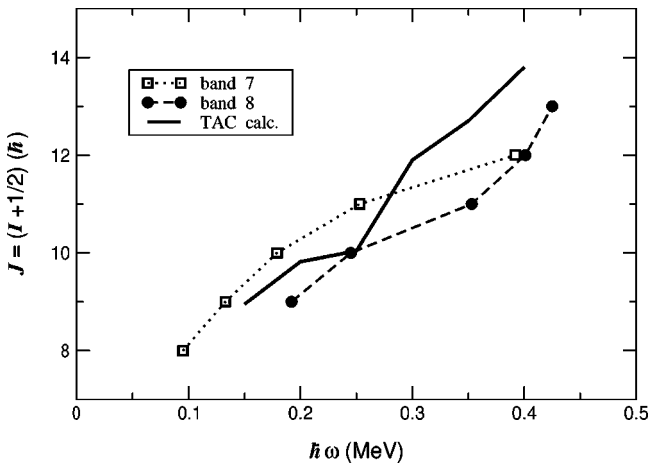

FIG. 9. Total angular momentum as a function of rotational frequency. The open squares and closed circles are the experimental data for bands 7 and 8, respectively, in ^{105}Rh. The thick line corresponds to the TAC calculations for the chiral $\pi g_{9/2}\otimes\nu h_{11/2}g_{7/2}$ excited configuration.

Normally some amount of collective rotation is necessary for the aplanar (or chiral) configuration to become favorable [10]. It is suggested, therefore, that bands 7 and 8 have the $\pi g_{9/2} \otimes \nu h_{11/2} g_{7/2}$ intrinsic chiral configurations. This will then be the first candidate reported on the experimental observation of a chiral doublet in an odd nucleus in this mass region (another candidate in an odd nucleus is recently reported in ^{135}Nd [38]). Due to the shallowness of the potential energy minima, the theoretical results become rather sensitive to the single particle energy parameters. It would be desirable, as more high-spin data from this mass region become available, to revise these parameters and improve the precision of the calculations.

V. CONCLUSIONS

The high spin states of the nucleus of ^{105}Rh have been measured and complemented. Four new structures were observed. A band (labeled 6), probably formed by the coupling of the $7/2^+[413]$ proton state $(\pi g_{9/2})$ to the $K^\pi = 2^+$ γ vibration of the core, was located. A multiplet of levels based on the $\pi\, 1/2^+[431]$ configuration has been identified and a related band structure (labeled 5) extended to $I^\pi = (27/2^+)$. A pair of structures (bands 7 and 8), previously unknown, are good candidates for the $\pi g_{9/2} \otimes \nu h_{11/2} g_{7/2}$ intrinsic chiral configurations, as predicted by TAC calculations. The measurement of transition probabilities and refined calculations would be very helpful to corroborate this suggestion and for a more conclusive configuration assignment for band 4.

ACKNOWLEDGMENTS

We thank the technical staff of the Pelletron Tandem Accelerator of the University of São Paulo. This work was partially supported by the Fundação de Amparo à Pesquisa do Estado de São Paulo (FAPESP) and the Conselho Nacional de Desenvolvimento Científico e Tecnológico (CNPq), Brazil. V.I.D. and S.F. acknowledge DOE Grant No. DE-FG02-95ER40934.

[1] H. Dejbakhsh, R. P. Schmitt, and G. Mouchaty, Phys. Rev. C **37**, 621 (1988).
[2] F. R. Espinoza-Quiñones, E. W. Cybulska, J. R.B. Oliveira, R. V. Ribas, M. N. Rao, M. A. Rizzutto, N. H. Medina, L. G. R Emediato, W. A. Seale, and S. Botelho, Phys. Rev. C **55**, 2787 (1997).
[3] F. R. Espinoza-Quiñones, E. W. Cybulska, J. R. B. Oliveira, R. V. Ribas, N. H. Medina, M. N. Rao, M. A. Rizzutto, L. G. R Emediato, W. A. Seale, and S. Botelho, Phys. Rev. C **55**, 1548 (1997).
[4] D. Jerrestam, W. Klamra, J. Gizon, F. Lidn, L. Hildingsson, J. Kownacki, Th. Lindblad, and J. Nyberg, Nucl. Phys. **A577**, 786 (1994).
[5] H. J. Keller, S. Frauendorf, U. Hagemann, L. Kubler, H. Prade, and F. Stary, Nucl. Phys. **A444**, 261 (1985).
[6] D. Jerrestam, W. Klamra, J. Gizon, B. Fogelberg, S. J. Freeman, H. J. Jansen, S. Mitarai, G. Sletten, and L. Thorslund, Nucl. Phys. **A579**, 256 (1994).
[7] S. Frauendorf, in *Proceedings of the International Symposium on In-Beam Nuclear Spectroscopy, Debrecen*, edited by Z. S. Dombrádi and T. Fényes (Akadémiai Kiadó, Budapest, 1984), p. 711.
[8] F. R. Espinoza-Quiñones, E. W. Cybulska, L. G. R Emediato, C. L. Lima, N. H. Medina, J. R. B. Oliveira, M. N. Rao, R. V. Ribas, M. A. Rizzutto, W. A. Seale, and C. Tenreiro, Phys. Rev. C **52**, 104 (1995).
[9] S. Juutinen, R. Julin, M. Piiparinen, P. Ahonen, B. Cederwall, C. Fahlander, A. Lampinen, T. Lönnroth, A. Maj, S. Mitarai, D. Műller, J. Nyberg, P. Šimeček, M. Sugawara, I. Thorslund, S. Trmnen, A. Virtanen, and R. Wyss, Nucl. Phys. **A573**, 306 (1994).
[10] S. Frauendorf and Jie Meng, Nucl. Phys. **A617**, 131 (1997).
[11] V. I. Dimitrov, S. Frauendorf, and F. Dönau, Phys. Rev. Lett. **84**, 5732 (2000).
[12] C. Petrache, D. Bazzacco, S. Lunardi, C. Rossi Alvarez, G. De Angelis, M. De Poli, D. Bucurescu, C. A. Ur, P. B. Semmes, and R. Wyss, Nucl. Phys. **A597**, 106 (1996).
[13] K. Starosta, T. Koike, C. J. Chiara, D. B. Fossan, D. R. LaFosse, A. A. Hecht, C. W. Beausang, M. A. Caprio, J. R. Cooper, R. Krűcken, J. R. Novak, N. V. Zamfir, K. E. Zyromski, D. J. Hartley, D. L. Balabanski, Jing-ye Zhang, S. Frauendorf, and V. I. Dimitrov, Phys. Rev. Lett. **86**, 971 (2001).
[14] K. Starosta, T. Koike, C. J. Chiara, D. B Fossan, and D. R. LaFosse, Nucl. Phys. **A682**, 375c (2001).
[15] R. A. Bark, A. M. Baxter, A. P. Byrne, G. D. Dracoulis, T. Kibdi, T. R. McGoram, and S. M. Mullins, Nucl. Phys. **A691**, 577 (2001).
[16] J. A. Alcántara-Núñez, J. R. B. Oliveira, E. W. Cybulska, N. H. Medina, M. N. Rao, R. V. Ribas, M. A. Rizzutto, W. A. Seale, F. Falla-Sotelo, F. R. Espinoza-Qiones, and C. Tenreiro, Nucl. Instrum. Methods Phys. Res. A **497**, 429 (2003).
[17] R. V. Ribas, J. R. B. Oliveira, E. W. Cybulska, M. N. Rao, W. A. Seale, M. A. Rizzutto, and N. H. Medina, Annual Report of the Nuclear Physics Department, Institute of Physics, University of São Paulo, 1996.
[18] W. T. Milner, *Holifield Heavy Ion Research Facility Computer Handbook* (Oak Ridge National Laboratory, Oak Ridge, TN, 1987).
[19] D. Radford, Nucl. Instrum. Methods Phys. Res. A **361**, 297 (1995).
[20] R. Duffait, A. Chavert, K. Deneffe, R. Beraut, A. Emsallem, M. Meyer, T. Ollivier, J. Treherne, A. Gizon, F. Beck, and T. Byrski, Nucl. Phys. **A454**, 143 (1986).
[21] J. Rogowski, N. Kaffrell, D. De Frenne, K. Heyde, E. Jacobs, M. N. Harakeh, J. M. Schippers, and S. Y. Van Der Werf, Phys. Lett. B **207**, 125 (1988).
[22] Ts. Venkova, M.-G. Porquet, I. Deloncle, B. J. P. Gall, H. De Witte, P. Petkov, A. Bauchet, T. Kutsarowa, E. Gueorgieva, J. Duprat, C. Gautherin, F. Hoellinger, R. Lucas, A. Minkova, N. Schulz, H. Sergolle, E. A. Stefanova, and A. Wilson, Eur.

Phys. J. A **6**, 405 (1999).
[23] Ts. Venkova, M.-G. Porquet, A. Astier, A. Bauchet, I. Deloncle, S. Lalkovski, N. Buforn, L. Donadille, O. Dorvaux, B. J. P. Gall, R. Lucas, M. Meyer, A. Minkova, A. Prvost, N. Redon, N. Schultz, and O. Stzowski, Eur. Phys. J. A **15**, 429 (2002).
[24] A. S. Davidov and G. F. Filippov, Nucl. Phys. **8**, 237 (1958).
[25] R. Bengtsson and S. Frauendorf, Nucl. Phys. **A327**, 139 (1979).
[26] R. Bengtsson and S. Frauendorf, Nucl. Phys. **A314**, 27 (1979).
[27] D. R. Haenni, H. Dejbakhsh, R. P. Schmitt, and G. Mouchaty, Phys. Rev. C **33**, 1543 (1986).
[28] R. Wyss, J. Nyberg, A. Johnson, R. Bengtsson, and W. Nazarewicz, Phys. Lett. B **215**, 211 (1988).
[29] W. Nazarewicz, J. Dudek, R. Bengtsson, T. Bengtsson, and I. Ragnarsson, Nucl. Phys. **A435**, 397 (1985).
[30] N. Kaffrell, P. Hill, J. Rogowski, H. Tetzlaff, N. Trautmann, E. Jacobs, P. De Gelder, D. De Frenne, K. Heyde, G. Skarnemark, J. Alstad, N. Blasi, M. N. Harakeh, W. A. Sterrenburg, and K. Wolfsberg, Nucl. Phys. **A460**, 437 (1986).
[31] N. Kaffrell, P. Hill, J. Rogowski, H. Tetzlaff, N. Trautmann, E. Jacobs, P. De Gelder, D. De Frenne, K. Heyde, S. Brjesson, G. Skarnemark, J. Alstad, N. Blasi, M. N. Harakeh, W. A. Sterrenburg, and K. Wolfsberg, Nucl. Phys. **A470**, 141 (1987).
[32] J. Rogowski, J. Alstad, M. N. Fowler, D. De Frenne, K. Heyde, E. Jacobs, N. Kaffrel, G. Skarnemark, and N. Trautmann, Z. Phys. A **337**, 233 (1990).
[33] G. Lhersonneau, B. Pfeiffer, J. Alstad, P. Dendooven, K. Eberhardt, S. Hankonnen, I. Klöckl, K.-l. Kratz, A. Nhel, R. Malmbeck, J. P. Omtvedt, H. Penttil, S. Schoedder, G. Skarnemark, N. Trautmann, and J. Yst, Eur. Phys. J. A **1**, 285 (1999).
[34] B. Gall, P. Bonche, J. Dobaczewki, and H. Flocard, Z. Phys. A **348**, 187 (1994).
[35] R. Bengtsson and J. D. Garret (unpublished).
[36] S. Frauendorf, Nucl. Phys. **A557**, 259c (1993).
[37] V. I. Dimitrov, F. Dönau, and S. Frauendorf, Phys. Rev. C **62**, 024315 (2000).
[38] S. Zhu *et al.*, Phys. Rev. Lett. **91**, 132501 (2003).